Student thesis series INES nr 663

Optimizing winter wheat leaf area index estimation across growth stages using UAV data

Ke Shao

2024

Department of
Physical Geography and Ecosystem Science
Lund University
Sölvegatan 12
S-223 62 Lund

Ke Shao (2024).

Optimizing winter wheat leaf area index estimation across growth stages using UAV data

Master degree thesis, 30 credits in *Physical Geography and Ecosystem Science*

Department of Physical Geography and Ecosystem Science, Lund University

Level: Master of Science (MSc)

Course duration: *January* 2024 until *June* 2024

Optimizing winter wheat leaf area index estimation across growth stages using UAV data

---

Ke Shao

Master thesis, 30 credits, in *Physical Geography*

Supervisor:

Shangharsha Thapa

Dept. of Physical Geography and Ecosystem Science, Lund University

El Houssaine Bouras

Center for Remote Sensing Application, Mohammed VI Polytechnic University

Lars Eklundh

Dept. of Physical Geography and Ecosystem Science, Lund University

Exam committee:

Zhanzhang Cai

Dept. of Physical Geography and Ecosystem Science, Lund University

Ross Petersen

Dept. of Physical Geography and Ecosystem Science, Lund University

Acknowledgements

I sincerely appreciate:

- My supervisors, for their invaluable guidance and support throughout this journey;

- My examiners and opponent, for their insightful suggestions;

- My friends and classmates, for their encouragement and friendship;

- My dear parents, for their unwavering support in every aspect of my life;

- And, the Department of Physical Geography and Ecosystem Science and Lund University, for providing me with this incredible opportunity.

Special thanks to myself, for the courage and perseverance that made all of this possible.

Abstract

Leaf Area Index (LAI) is an important parameter for monitoring vegetation status and estimating crop yield, essential for precision agriculture, forestry and natural resource management. Therefore, estimating the LAI with high spatial resolution and temporal flexibility is crucial for providing precise and timely information to make informed decisions. This study focuses on optimizing the estimation of LAI in winter wheat across different growth stages by integrating spectral data and plant height, with a high spatial resolution of 4 cm × 4 cm and 5 cm × 5 cm respectively, which derived from Unmanned Aerial Vehicle (UAV) imagery. The research investigates which spectral bands or vegetation indices (VIs) are most effective for LAI estimation, the variability of LAI estimation across growth stages, and the enhancement of LAI estimation through the addition of plant height data. The result of the coefficient of determination (R^2) showed that the Normalized Difference Red Edge (NDRE) was the most effective single feature for LAI estimation (R^2 = 0.64), followed by the Chlorophyll index with red edge (CIrededge) with an R^2 of 0.56, while red edge (REG) reflectance showed limited predictive capability (R^2 = 0.01). Models incorporating multiple features generally improved estimation accuracy, demonstrating the benefit of multi-feature models. The combination of height and CIrededge achieved the highest predictive accuracy and lowest error rates for multi-feature models, with an R^2 of 0.82 and a root mean square error (RMSE) of 0.37 m^2/m^2. Growth stage-specific models further refined LAI estimation, with vegetative and productive stages showing distinct performance variations. The study concludes that NDRE can estimate LAI with a high accuracy overall while integrating the CIrededge and height data from UAVs enhances the precision of LAI estimation significantly, and the consideration of growth stages is necessary.

Keywords: LAI, multispectral UAV, winter wheat, machine learning, Random Forest

List of abbreviations:

B	Blue band
CIrededge	Chlorophyll index with red edge
DSM/DSMs	Digital Surface Model/Digital Surface Models
G	Green band
LAI	Leaf area index
MAE	Mean absolute error
MSE	Mean square error
NDRE	Normalized difference red edge
NDVI	Normalized difference vegetation index
NIR	Near-infrared band
R	Red band
REG	Red edge band
RMSE	Root mean square error
R-Square/R2	Coefficient of determination
SWIR	Shortwave infrared band
UAV	Unmanned aerial vehicle
VI/VIs	Vegetation index/Vegetation indices

Table of Contents

1. Introduction 1
2. Background 4
2.1 Growth stage of winter wheat 4
2.2 LAI and crop growth monitoring 4
2.3 Vegetation index and remote sensing 4
2.4 Methods to estimate LAI 5
3. Materials and methods 7
3.1 Study area 7
3.2 Field data measurements 7
3.2.1 Field LAI data collection 10
3.2.2 Field wheat height data collection 11
3.3 UAV Data collection and processing 11
3.4 UAV data calculation 15
3.4.1 Reflectance and Vegetation Indices (VIs) extraction 15
3.4.2 Wheat height estimation 16
3.5 Model building and evaluation 18
3.5.1 Data distribution 18
3.5.2 Correlation analysis 19
3.5.3 Model establishment 19
3.5.4 Model validation 20
4. Result 23
4.1 Wheat height estimation from UAV data 23
4.2 Time series analysis 24
4.3 The correlation between LAI and variable 26
4.4 LAI estimation using single model 27
4.5 Model based on growth stage 30
5. Discussion 33
5.1 Weather impacts on LAI 33
5.2 Uncertainties of plant height data 33
5.3 Model overfitting 34
5.4 The availability of REG band 34
5.5 Impaction of the radiometric calibration 35
6. Conclusion 38
Reference 39
Appendix I

1. Introduction

Winter wheat (*Triticum aestivum L.*) is a commonly grown grain crop in Europe (Kristensen et al., 2011). The entire growing cycle of winter wheat begins from the vegetative phase, then to the early reproductive phase and late reproductive phase, plus the stage of grain filling complete one growing cycle (Slafer et al., 2021). In Northern Europe, winter wheat is usually sown from mid to late September and initiates the tillering before the winter dormancy period. As light and temperature conditions become suitable, winter wheat greens up and progresses into the reproductive phase. This period is called the vernalization. Harvesting of winter wheat generally occurs from late July to early August.

According to the Eurostat (EuropeanCommission, 2024) common wheat and spelt account for about 43% total Europe's annual production of main cereals (2019-2021 average). Within the common wheat and spelts category, winter wheat took over 96% of the total production which was one very important main food supplement. In Sweden, winter wheat accounted for approximately 51% of the total cereals production in 2022, with a yield of 3.018 million tonnes (SCB, 2023). However, the stability of grain production is under the threat of global warming, which has been proven that climate change can lead to a change in wheat yield (Faye et al., 2023; Webber et al., 2018). Therefore, monitoring the growth status of winter wheat to achieve the expected yield is crucial for ensuring food security.

Over the years, various methods have been developed to ensure the healthy growth of winter wheat and accurately estimate its final yield. From the early use of radar to estimate plant moisture content (BUSH, 1976) to the more recent development of spectral vegetation indices for detecting wheat diseases (Ashourloo et al., 2014), these techniques cover a wide range of applications and have significantly advanced our understanding of wheat crop management. Among them, the leaf area index (LAI) which is defined as the sum of green leaf area per unit area of land (WATSON, 1947) has become a common and useful variable for monitoring crop growth, health and production. Since the LAI of winter wheat exhibits systematic variations within a certain range in different growth stages, monitoring changes in LAI can be used to assess its growth status, especially in assisting the final yield prediction (Kanning et al., 2018). The direct method of LAI estimation is to cut off every leaf within one unit

area and sum up the areas of these cut-off leaves, which provides the most precise LAI value. It is suitable for a small range of measurements but when the monitoring range is larger than a couple of fields, it is very common to use indirect methods to estimate LAI. Indirect methods generally analysed the relationship between the LAI and other variables which are more easily to obtain.

Variables such as various vegetation indices can be acquired through remote sensing. Satellite remote sensing as the most typical remote sensing method has a large-scale temporal and spatial extent. However, satellite remote sensing commonly with a low spatiotemporal resolution. Furthermore, the vast distance between satellites and observed objects also results in images being greatly affected by weather conditions such as the block of the clouds. So, there will be a data gap for overcast days. In this study which aims to monitor LAI on a field scale and at high spatial resolution, a high precision is necessary. Thus, satellite remote sensing is not the best option. On the contrary, unmanned aerial vehicles (UAV) remote sensing, with its high spatial resolution and flexibility in time and location, is more suitable for small-scale areas.

Since the VIs are computed based on the radiation reflectance of the plants, the abnormal values often represent the suboptimal health status of plants. Besides VIs combined different bands can overcome the limitations of the single band (Fang et al., 2019). Based on the usage, UAV can be equipped with different sensors to compute different VI. For example, Yan et al. (2022) chose sixteen common VIs to estimate cotton LAI. Many researchers have analysed the relationship between VIs and LAI. The common models for estimating the LAI include simple linear, polynomial, exponential, or logarithmic relationships (Qi et al., 1994). More sophisticated methods such as using machine learning to build the regression model have been widely used these years (Fang et al., 2019). For it can not only handle complex associations between many variables (Azadbakht et al., 2019) but can provide a better regression model for the large dataset.

The main aim of this study is to optimize the accuracy of LAI estimation of winter wheat across growth stages at high spatial resolution. By using UAV remote sensing, the data can be captured on flexible dates according to the actual usage. So, the study will focus on a better understanding of the variables which can be used to estimate LAI or will influence the measurement of LAI from UAVs in different growth stages.

The possible variables are the VIs based on the red edge band (REG) and near-infrared band (NIR); and the plant height based on the UAV-derived digital surface model (DSM).

The following questions will be answered:

(1) Which spectral band or which VI perform the best in estimating winter wheat LAI?

(2) Does the estimation of LAI vary across different growth periods?

(3) Does the addition of the plant height enhance the LAI estimation?

2. Background

2.1 Growth stage of winter wheat

The growth stage can be defined on a quantified scale make ensure the consistency of the winter wheat across different times, locations, cultivation methods, and various species. According to Zadoks growth scale, winter wheat together with other cereal crops have ten principal growth stages which are: 0- Germination; 1- Seeding growth; 2- Tillering; 3- Stem elongation; 4-Booting; 5- Ear emergence; 6- Flowering (anthesis); 7- Milk development; 8- Dough development; 9- Ripening (Zadoks et al., 1974).

2.2 LAI and crop growth monitoring

According to Watson (1947), the leaf area index has been defined by summing all of the leaf areas within one unit area of land. In other words, in one unit area, the more leaves area it has, the higher LAI it will be. Since plants acquire energy and accumulate carbon through photosynthesis conducted by the green leaves, the value of LAI can indicate the growing condition of the vegetation. When the plants are under water and nutrition stress, insect and disease attacks and unsuitable weather, the number and area will change thus leading to the changing of the LAI. Monitoring the changing of LAI during the growing season can help understand crop growth status, optimize the irrigation and fertilization of the farmland and inspect the negative factors in an early stage (Cheng et al., 2024). LAI also has been widely used to estimate the biomass, chlorophyll content and yield of crops (Yu et al., 2023). By measuring LAI regularly, farmers can optimize field management and predict the potential yield which can minimize planting expenses and mitigate resource inefficiencies to increase the financial returns.

2.3 Vegetation index and remote sensing

Vegetation absorbs a portion of solar radiation while simultaneously reflecting other parts of the electromagnetic spectrum. Water accounts for 50% to 80% of the leaf's fresh weight which leads the leaf to absorb more electromagnetic radiation in NIR (700 – 1300 nm) and shortwave infrared (SWIR, 1400 – 3000 nm) wavelengths (Liu et al., 2016). Besides, plant leaves contain plant pigments, particularly chlorophyll, absorbing the blue and red regions of the visible waveband (450 – 495 nm and 620 –

750 nm) strongly while performing high reflectivity and transmissivity in the green band (495 – 570 nm) (Arkebauer, 2005). Based on reflectance characteristics, different bands can be combined in many ways according to the specific objectives (Foley et al., 1998).

Remote sensing detects and records the reflectance information by using passive sensors on the remote sensing equipment at a distance (Xue & Su, 2017). Therefore, spectral characteristics changes of green leaves, canopy and the soil are the common objectives for vegetation remote sensing. Because the canopy is a collection of leaves, the canopy spectral reflectance is functionally linked to the LAI which has been researched by many studies in recent years (Haboudane et al., 2004).

2.4 Methods to estimate LAI

The main categories for methods to estimate LAI include direct, semi-direct and indirect methods.

The direct method or the traditional method provides the real LAI which is only related to foliage (Bréda, 2003). In this method, LAI is simply computed by summing up the areas of all cut-off leaves within one unit area. The direct method can be very precise but needs to destroy the samples and thus cannot be used at a high frequency. It also cannot be used on a large scale because it highly depends on human labour and consumes time. The way to choose the samples can lead to a high deviation result so the direct method always needs several repetitions to reduce the errors (Černý et al., 2020). Moreover, the limited dataset size further constrains relevant research avenues.

Based on the direct method, the semi-direct methods can estimate LAI by correlating the LAI with plants' dry mass (Bréda, 2003) or counting the number of leaves that touched a vertical probe equipment (Wilson, 1960) without cutting the plants every time. Semi-direct method can not only decrease the disruption to the plants but relatively reduce the workload as well. However, the method still can only focus on the selected time and points which is not suitable for large scale or high temporal resolution.

Indirect methods estimate LAI by establishing and utilising mathematical models to predict LAI. Unlike the direct or semi-direct methods, indirect methods do not harm the plant and can be used with a range of scales. They can be divided into the

proximal and remote sensing methods, deriving the LAI according to some more easily measurable parameters (Černý et al., 2020). The proximal methods are using an active sensor such as the spectrometer to measure the radiometric reflectance or using a digital camera to take plant images to calculate the gap fraction (Yang et al., 2023). The remote sensing methods measure and acquire the radiometric data at a distance. Based on the radiometric data, the VIs and texture features can be calculated and extracted. Many papers have described the variation of different VIs and different vegetations (Qiao et al., 2022) and have extracted six texture features to analyse maize LAI. And for the gap fraction computed from the cameras, can be used as the independent variable in the Beer–Lambert law which defines the relationship between the gap fraction and LAI (Yang et al., 2023).

Among these methods, spectrometers and digital cameras are mostly used in field work to compute the ground truth LAI. Remote sensing techniques such as drones and satellite RS are more suitable for establishing predictive models on larger temporal and spatial scales. Due to its multispectral bands and diverse products, satellite remote sensing has been widely used to compute various VIs. However, the data is sensitive to weather conditions (Yan et al., 2022). Furthermore, the low spatial resolution restricts its estimation precision on LAI and the fixed orbit restricts the temporal flexibility of satellite remote sensing data acquisition. UAV is often chosen to estimate field scale LAI in order to ensure the timeliness of data and the accuracy of prediction. Depending on the budgetary constraints and research objectives, UAVs equipped with varying sensors can be selected accordingly.

3. Materials and methods

3.1 Study area

The study was conducted in Alnarp on the three rainfed winter wheat fields in Southern Sweden (Figure 1). The area is characterized with a relatively flat terrain. The mean annual temperature and precipitation (1981- 2010) are around 8 °C and 5500-750 mm (Williams et al., 2020) in this region (Skåne County). In 2023, over 40% of the agricultural area in Skåne was used for grain plants, and 46% of the grain farmland was used for planting winter wheat (JordbruksverketsStatistikdatabas, 2023).

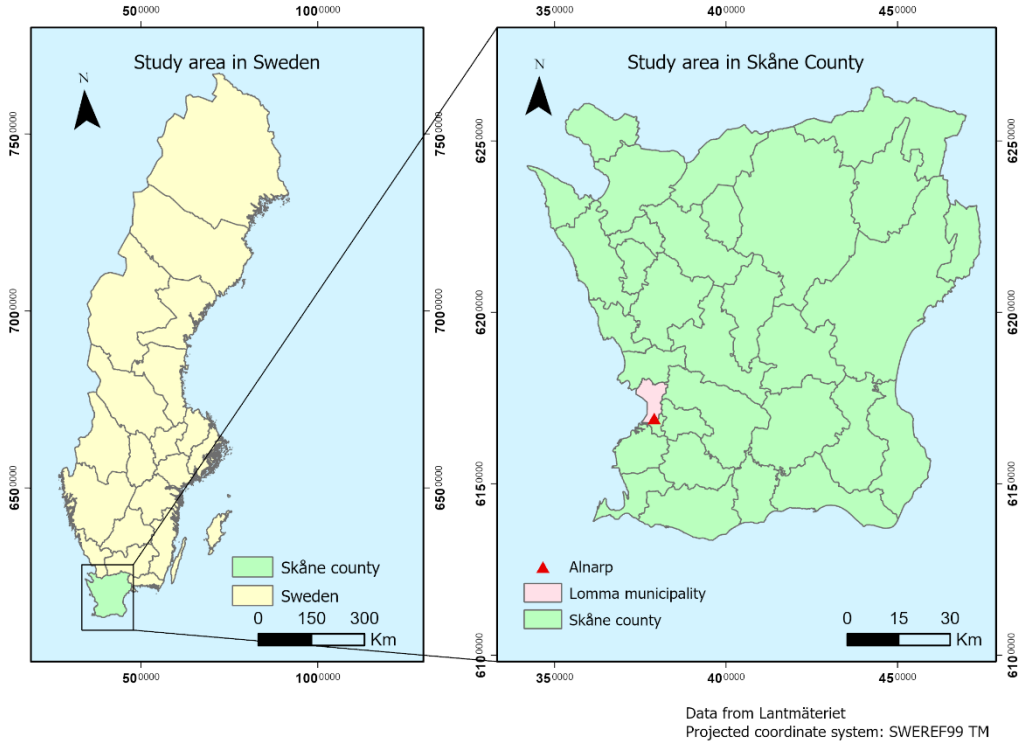

Figure 1. *Study area in Sweden map and local county map. Fields are located in Alnarp, southwest Skåne, south Sweden. Coordinates are displayed in the projected Coordinate System SWEREF99 TM.*

3.2 Field data measurements

Field data included wheat LAI and wheat height, collected during almost the entire growing season (from April to July) at approximately two-week intervals. The growth stage of wheat at each sampling time was defined based on the Zadoks growth scale (Zadoks et al., 1974), which allowed the analysis of changes in LAI and various

variables during different growth periods. Based on the date of sowing in the experimental fields and the phenological characteristics, the rough growth stages with the date of each field data measurement are displayed in Table 1. The example photos of four representative growth stages are displayed as oblique images (Figure 2). Since the data was collected about every other week, there was no specific data for the 'Ear emergence' period and 'Flowering' period. Instead, the data indicated a middle stage of these two periods.

Field data were collected within three experimental fields in this study (Figure 3). Every field had two measurement sampling plots. The size of each of the sampling plots was approximately 50 × 50 square meters. Every sampling plot contained five sampling points (four on each vertex and one on the centre) and there were two separate sampling points distributed among the experimental field one. In summary, the total number of samples was 32 (Table 1), where field one had 12 sampling points, and fields two and three both had 10 sampling points. The distribution of sampling plots is displayed in Figure 3. On each sampling point, a flag marked with a sample identifier was fixed in the soil to ensure location consistency. The sampling point number and its specific coordinates can be found in Appendix 1.

Table 1. *Date and growth stages of field measurement for winter wheat. 'Nr.' Represents 'The number'.*

Nr. of field measurement	Date	Zadoks growth scale	Nr. of sample points
1	April 5, 2023	2- Tillering	32
2	April 20, 2023	3- Stem elongation	32
3	May 3, 2023	3- Stem elongation	32
4	May 17, 2023	4- Booting	32
5	May 24, 2023	4- Booting	32
6	June 7, 2023	5- Ear emergence 6- Flowering	32
7	June 20, 2023	7- Milk development	32
8	July 4, 2023	8- Dough development	32
9	July 18, 2023	9- Ripening	32

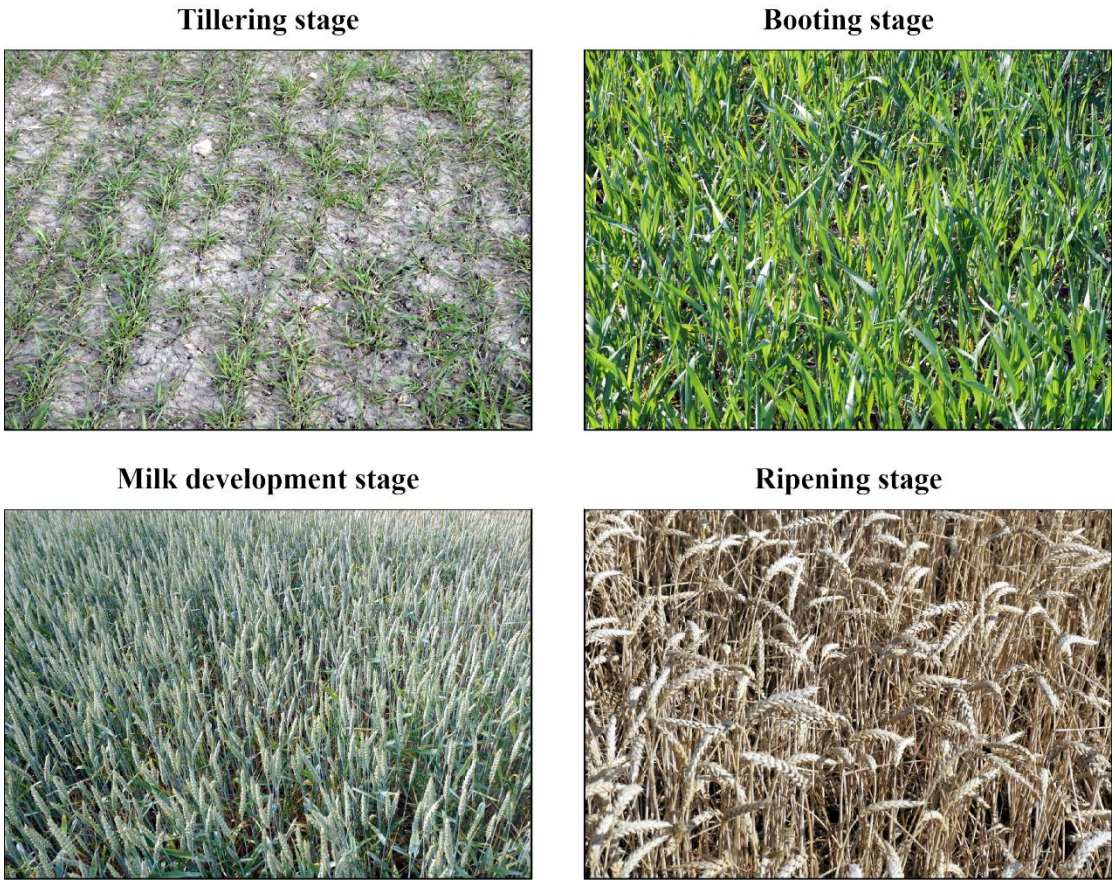

Figure 2. *Oblique images of winter wheat of various growth stages.*

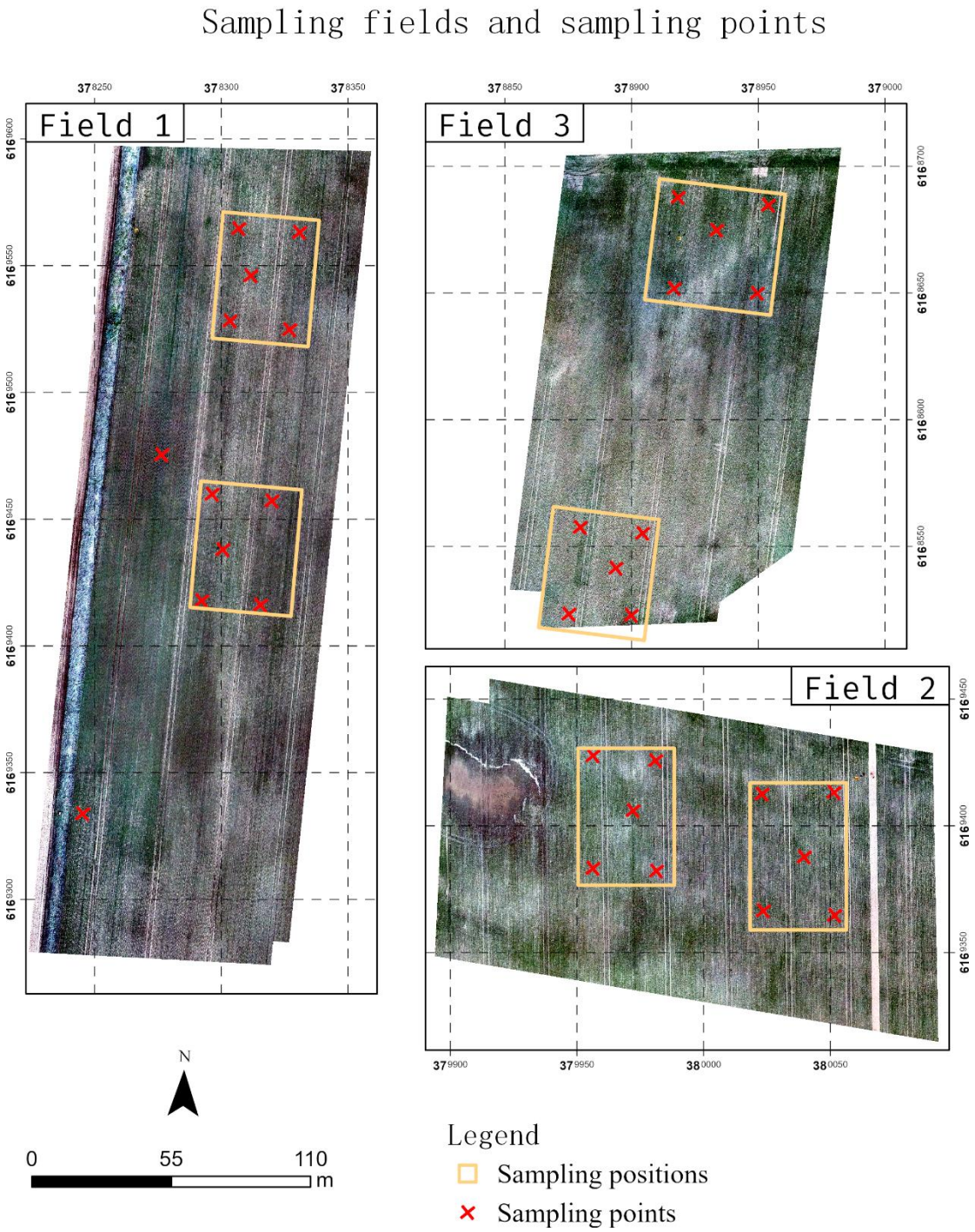

Figure 3. *Orthomosaic image of three experimental fields in 2023, displaying the location of 32 sampling points for this study. Coordinates are displayed in the projected Coordinate System SWEREF99 TM. Field 1 includes sampling plots 1 (north) and 2 (south); field 2 includes sampling plots 9 (west) and 10 (east); field 3 includes sampling plots 17(north) and 18(south).*

3.2.1 Field LAI data collection

Field LAI data was used to train and test LAI estimation models. It was computed through oblique images which were taken by RGB camera (a-6000, SONY). At each

point, oblique images were taken at the place of each sampling point's flag marker twice. The camera was mounted on a tripod with a bubble level to ensure its horizontal position. During every measurement, the camera took two images in opposite directions whose orientations were perpendicular to the sunlight to avoid shadow effects. Additionally, the camera captured images at a 57.5-degree zenith angle. The oblique images were then processed by the UPSCALE project of the department through the software CAN-EYE V6.4.7 (French National Institute of Agronomical Research, 2003) to compute wheat LAI.

3.2.2 Field wheat height data collection

Wheat height was defined as the distance from the ground to the highest point of the plant (Jamil et al., 2022). The field wheat height data in this study referred to the ground truth height which was measured manually in the field. They were measured by a scale with a 1-millimetre graduation value. The field height of winter wheat was measured on the same day as the acquisition of oblique images. Similar to the method previously described for capturing oblique images, the height of two randomly selected plants on each side of the sample point, perpendicular to the incident sunlight, was measured. Therefore, four plant heights were measured at each sample point, and the average value was calculated to represent the height at that sampling point. Field wheat height was used as height reference when estimating height by using the UAV images in order to evaluate the accuracy.

3.3 UAV Data collection and processing

The UAV data used in the study were images taken by a P4 Multispectral DJI drone. UAV images were collected approximately the same day or one day after each field measurement. The dates of flights are displayed in Table 2 which contains the detailed weather conditions as well. Additionally, there were no other flights between 17th May and 6th June. So, for field data collected on 17th May and 24th May (Nr. 4 and 5 of field measurement), the UAV data was the same (Nr. 4 of UAV collection).

Table 2. *Date of UAV flights and weather conditions. Mixed weather means both have sunny and cloudy conditions. 'Nr' Represents 'UAV data collection number'.*

Nr.	Date	Field 1	Field 2	Field 3

1	April 5, 2023	sunny	sunny	cloudy
2	April 21, 2023	cloudy	cloudy	cloudy
3	May 4, 2023	mixed	cloudy	cloudy
4	May 21, 2023	sunny	sunny	mixed
5	June 8, 2023	cloudy	cloudy	cloudy
6	June 21, 2023	mixed	mixed	sunny
7	July 7, 2023	mixed	sunny	mixed
8	July 21, 2023	sunny	sunny	mixed

Regarding the UAV images, the drone had a multispectral camera array with five monochrome sensors (red, green, blue, red edge and near-infrared) and one RGB camera for visible light imaging. Each time when the drone took a shot, images of five bands were saved individually in the memory card of the drone. At the same time, the RGB camera automatically generated a true colour image which was also stored in the memory card. The detailed information on each band is displayed in Table 3.

Table 3*. The wavelength ranges of each band for individual sensors. Data download from DJI official website (https://www.dji.com/se/p4-multispectral/specs, accessed on 30 March 2024).*

Band name	Abbreviation	Wavelength range
Blue	B	450 nm ± 16 nm
Green	G	560 nm ± 16 nm
Red	R	650 nm ± 16 nm
Red edge	REG	730 nm ± 16 nm
Near-infrared	NIR	840 nm ± 26 nm

All flights were done in pre-programmed flight paths between 10 am and 3 pm to maintain the relative stability of image range and solar radiation. Before every flight, three reflectance panels with 9%, 23% and 44% reflectance were laid out on the ground on top of the green tarp. The flying height of the drone was set at 40 meters above the ground level and reflectance panel images were captured both before and after each flight mission. At least three reflectance panel images were acquired with panel centred on each of these images which was later used for radiometric calibration. Then the drone flew at the planned route to collect images. The front overlap was set

to 80% and the side overlap was 60%. Every flight had the same parameters and settings to control the variables.

After completing the flight mission, UAV photos collected were downloaded to the computer to perform image processing. For every single spectral band and RGB images captured in each flight, they were processed separately with the method explained in (Thapa et al., 2021). The same steps were applied to process other flights too. The flow chart of UAV image processing (Figure 4) is shown below. First, photos took by UAV were pre-processed. Photos that focused unproperly were removed. Besides, for flights that under mixed weather conditions, irradiance data from all images of the flight was retrieved and plotted to check the consistency. The irregular plots together with the images were removed. The rest of the irradiance data was normalised according to the light and weather conditions (Olsson et al., 2021). Second, images after pre-processing were orthomosaiced and subjected to the next step according to the different aims. The resolution of the orthomosaic maps was 5 cm. The pre-processing and image orthomosaic preparation was carried out by the UPSCALE project at the department, which provided multispectral images and DSMs as well.

For generating the reflectance map, orthomosaic maps needed to be calibrated radiometrically. The radiometric calibration was done by using the empirical line corrections method which constructs a linear relationship between the mean pixels value of the reflectance panels in the image and the standard reflectance of the panels. The DN values were extracted by drawing the region of interest manually on the reflectance panels first (Figure 5) and then computing the average (Olsson et al., 2021). Next, based on the average DN values and the standard reflectance of each panel, a linear equation was calculated. In this experiment, the raw orthomosaic was calibrated using the derived equation, thereby producing a reflectance map. The plant height map was generated from the crop surface model which is a digital surface model obtained from the photogrammetric process.

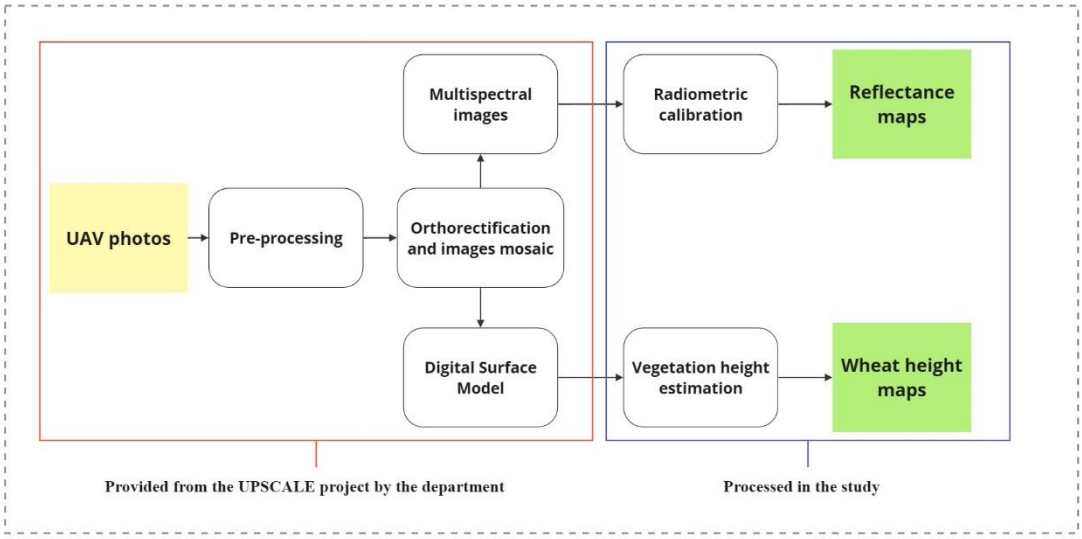

Figure 4. *The diagram with steps of UAV image processing.*

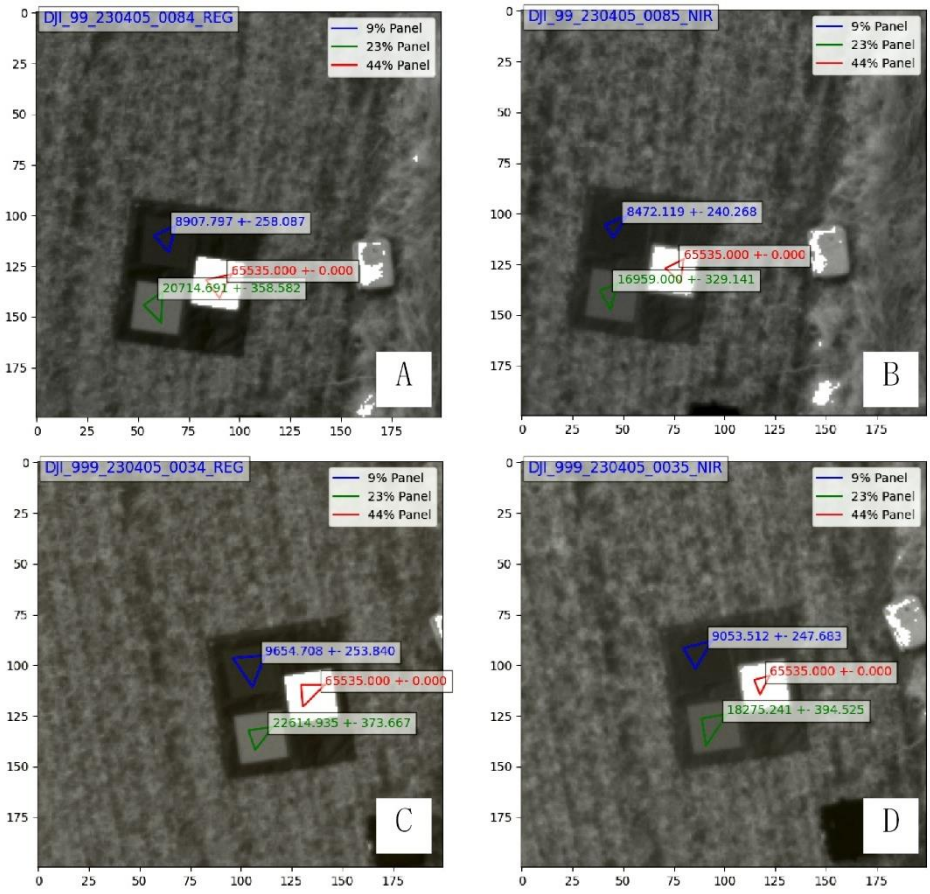

Figure 5. *Example of extracting digital number on reflectance panel from DN map. Figure A and B were captured before the flight mission, while Figure C and D were captured after the flight route. A and C were in the red-edge band, B and D were in the near-infrared band. Images captured on 5th April, 2023.*

3.4 UAV data calculation

VIs and reflectance data were then calculated and extracted based on processed UAV reflectance maps. Wheat height data were computed based on DSMs.

3.4.1 Reflectance and Vegetation Indices (VIs) extraction

The study computed vegetation index CIrededge and NDRE based on the calibrated data. Both CIrededge and NDRE are sensitive to chlorophyll content in plant leaves which is a key component of photosynthesis (Steele et al., 2008; Xie et al., 2018). Higher chlorophyll content typically indicates a higher LAI.

According to the coordinates of sample points measured before, a three-meter radius buffer was created around each sample point (Figure 6). Average spectral values of REG and NIR within each buffer were extracted then. Then two vegetation indices were computed and extracted in the same way. The name and the computing formula of the VIs can be seen in Table 4.

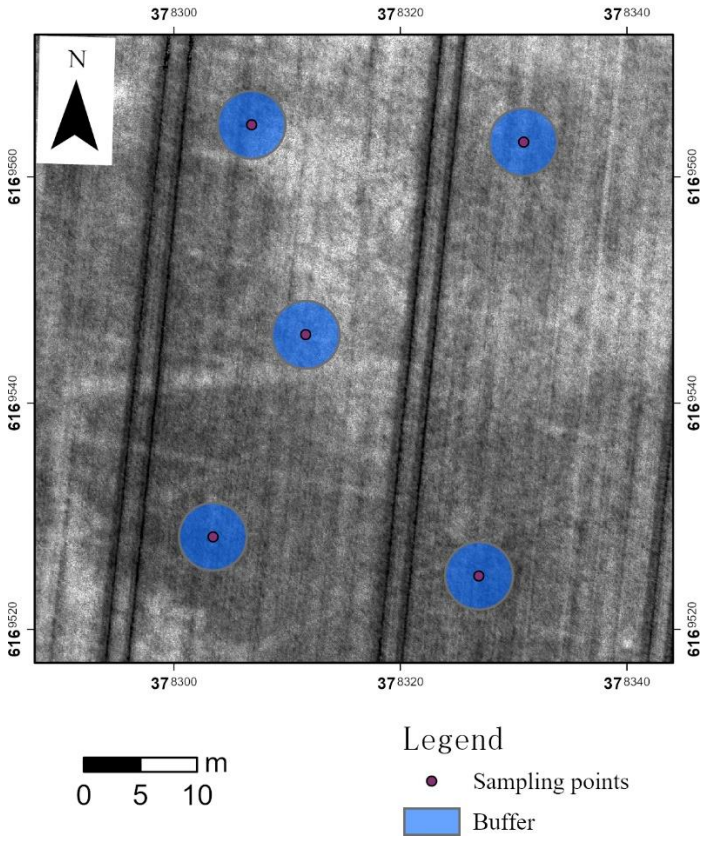

Figure 6. *Example of buffer area. Background map was the chlorophyll index with red edge on 21st May,2023, sampling points (P01-1, P01-2, P01-3, P01-4, P01-5) were in position one.*

Table 4. *Vegetation indices used in this study*

Name	Abbreviation	Equation	Reference
Chlorophyll index with red edge	CIrededge	$\frac{NIR}{REG} - 1$	(Pôças et al., 2020)
Normalized difference red edge	NDRE	$\frac{(NIR - REG)}{(NIR + REG)}$	(Li et al., 2014)

3.4.2 Wheat height estimation

In this study, wheat height was estimated by computing the DSMs difference between the base layer and flights by using ArcGIS Pro 2.7 (Esri, 2020). The baseline layer here indicated the DSMs constructed by the first flight (flight of 5th April 2023). To compute the difference, DSMs values of flights and sample points needed to be extracted. Processes for extracting average DSM values are displayed in the diagram below (Figure 7). In general, the method for extracting DSM at sample points was similar to that used for extracting VIs, wherein constructed a 3m radius buffer around each sample point. However, due to the influence of non-vegetated areas within the buffer on the DSM values, the average plant height was lower than the actual height. Therefore, this study composited Normalized Difference Vegetation Index (NDVI, Equation 1) maps based on DN values. Because NDVI could distinguish vegetation from various landcover effectively with high precision (Huang et al., 2021). Regions with NDVI values greater than a threshold were then classified as vegetation. The thresholds were defined according to the NDVI time series of winter wheat (Dong et al., 2019; Li et al., 2021) and displayed in Table 5.

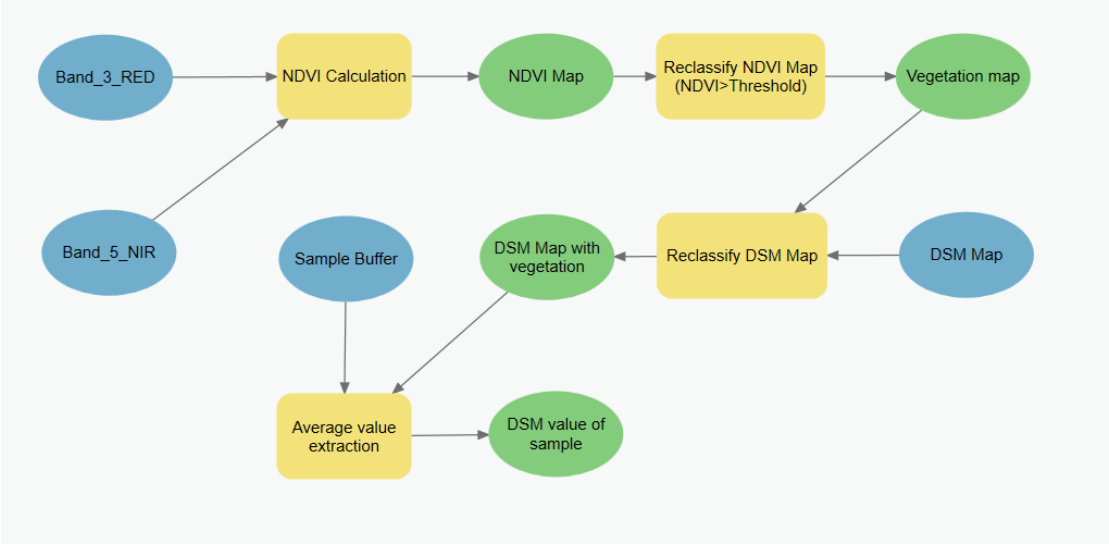

Figure 7. *Diagram of extracting digital surface model value of samples. The circles represent data, with blue indicating input data, and green indicating intermediate and output data respectively. The yellow rectangles represent the calculation. Some of the intermediate data was used as input data as well.*

Table 5*. Date of UAV flights and normalized difference vegetation index threshold when classifying vegetation and other land cover. Normalized difference vegetation index higher than the threshold was considered a plant. 'Nr' Represents 'The flight number.*

Nr.	Date	Threshold	Nr.	Date	Threshold
1	April 5, 2023	0.2	5	June 8, 2023	0.5
2	April 21, 2023	0.2	6	June 21, 2023	0.3
3	May 4, 2023	0.5	7	July 7, 2023	0.2
4	May 21, 2023	0.5	8	July 21, 2023	0.2

After classifying the data, the average DSM value for the vegetation within the buffer zone of each sample point was extracted. Subsequently, the difference in average DSM values between the flights and the baseline layer was calculated. This difference was then added to the baseline plant height, which was the measured wheat height in the field as of April 5th, 2023. This approach allowed for the estimation of plant height for each flight. The height estimation method is represented in Equation 2 below.

$$NDVI = \frac{(NIR - R)}{(NIR + R)} \qquad Equation\ 1$$

$$Plant\ height = \left(DSM_{t_n p_i} - DSM_{t_1 p_i}\right) + H_{p_i} \quad , for\ n \in [2,8]\ and\ i \in [1,32]$$

$$Equation\ 2$$

where $DSM_{t_n p_i}$ represents the DSM value at the nth time flight and sample point P_i, $DSM_{t_1 p_i}$ represents the DSM value at the initial time and sample point P_i, $H_{t_1 p_i}$ represents the field plant height of April 5th, 2023 at sample point P_i, n ranges from 2 to 8, indicating the flight number, i ranges from 1 to 32, indicating sample point number.

After estimating plant height, the study did the linear regression analysis to quantitatively assess the relationship between the estimated plant height values and the actual measured plant height values. The analysis could validate the reliability of the estimated plant height.

3.5 Model building and evaluation

The final dataset included LAI data and variables data for the year 2023. Variables included single band REG and NIR, VIs CIrededge and NDRE, and wheat height. LAI data were computed based on REG images taken from the camera. Spectral-related data including single band data and VIs were obtained and computed from UAV images. The total number of sampling data was 288, which was collected in 32 sampling spots and covered eight growth stages of winter wheat (tillering, stem elongation, booting, ear emergence, flowing, milk development, dough development and ripening). However, due to influences such as unstable weather conditions and insufficient battery power of the equipment, there was an LAI data gap on 17th May and a UAV data gap on 4th July. Therefore, a total of 268 data was used in this study.

3.5.1 Data distribution

Before analysing the correlation, it was important to see the distribution pattern of LAI and variables for different growth stages. Took the average of LAI and variable value for every sampling time and distributed the data in a time series. Some growth stages had more than one sampling time, so mean LAI and variable value were also computed according to the growth stage and distributed in a time series.

Variable or LAI might display a consistent increase or decrease over time or display a parabola shape with the growth of crops. Based on the distribution characteristics of LAI, all data or part of the data were applied to analyse the correlation which ensured variable remained consistent with LAI. For those data that have been segmented, correlation with LAI was analysed separately.

Due to the saturated value of reflectance panels in red, green and blue bands, only the REG band and NIR band managed to be calibrated, which has limited the usable of VIs. Therefore, the study also analysed and compared the distribution of DN value with reflectance, which can give information regarding to the possibility of using DN value to estimate LAI.

3.5.2 Correlation analysis

In order to assess the relationship between LAI and variables, the study computed both the Pearson correlation coefficient and the Spearman correlation coefficient. Since the data's characteristics encompassed both standard and non-standard normal distributions, with and without outliers. Pearson correlation coefficient can measure the strength of the linear relationship between LAI and a variable and is sufficient when data is in normality distribution (Hauke & Kossowski, 2011). Spearman correlation coefficient has the advantage that it is not sensitive to outlier data and not a linear relationship measurement between LAI and one variable (Croux & Dehon, 2010). Based on the correlation coefficient, a strong correlation (correlation coefficient >= 0.75) with high statistically significant (P-value < 0.05) between the variable and LAI implied a good performance of the model. Because it would be able for the machine learning algorithm to learn some correlated information from the data. Therefore, the variable was considered a usable feature of models.

3.5.3 Model establishment

Although the entire dataset contained 268 data, however, when data corresponding to LAI values equal to zero, which indicated there was no green leaf existed, were considered invalid. So, a total of 233 data was used as input data to establish the model. And ripening stage was excluded to estimate LAI because LAI was always zero in this stage.

Input data for the models mentioned above was divided into training dataset and testing dataset. It was done by random split method which randomly allocated input data into the training dataset and testing dataset with an 8:2 proportion.

The study used the Random Forest algorithm (Breiman, 2001) to obtain the regression model between LAI and variable(s). The Random Forest approach which was developed from a decision tree is widely used to deal with data with many features. Each variable was considered as one feature when establishing models.

For LAI estimation using single model, all growing stages data was used. Model was constructed by using one feature first. More features were added based on the results obtained from the initial models and the correlation between features and LAI. For model based on growth stages, data of each growth stage was used respectively. The result from the model in each growth stage could show which variable were most useful to estimate LAI in a certain period.

3.5.4 Model validation

Performance metrics are an essential component of quantifying the estimation performance of models. When using machine learning methods for regression analysis, metrics are used to compare the difference between the predicted values from the model and the actual values from the measurements (Botchkarev, 2018). Both training data and testing data can be used to compute metrics depending on the aim. The most commonly used metrics are mean absolute error (MAE), mean square error (MSE), root mean square error (RMSE) and the coefficient of determination (R-Square/R^2).

The formulas of metrics can be seen below, where y_i is the true value for the i^{th} observation, $\hat{y}_i$ is the predicted value for the i^{th} observation, $\bar{y}$ is the average of the true values and n is the number of observation samples.

$$MAE = \frac{1}{n}\sum_{i=1}^{n}|(y_i - \hat{y}_i)| \qquad Equation\ 3$$

$$MSE = \frac{1}{n}\sum_{i=1}^{n}(y_i - \hat{y}_i)^2 \qquad Equation\ 4$$

$$RMSE = \sqrt{\frac{1}{n}\sum_{i=1}^{n}(y_{i-}\hat{y}_i)^2} \qquad Equation\ 5$$

$$\text{R-Square/R}^2 = 1 - \frac{\sum_{i=1}^{n}(y_{i-}\hat{y}_i)^2}{\sum_{i=1}^{n}(y_{i-}\bar{y})^2} \qquad Equation\ 6$$

MAE (Equation 3) simply calculates the absolute differences between predicted and actual values and then takes the average of the differences. It is easy to interpret and not sensitive to outliers (Chai & Draxler, 2014). The smaller the MAE is, the better the predicted results made by models there will be. MSE (Equation 4) and its rooted variant RMSE (Equation 5) are calculated in a similar way as MAE which takes the average of squared differences between the predicted values and the measurement value. MSE and RMSE are more sensitive to outliers and ambiguous when interpreting their meaning (Cort & Kenji, 2005). However, Chai and Draxler (2014) have proved that MSE and RMSE can represent model performance well for error in Gaussian distribution. The lower RMSE represents a smaller dispersion of experimental results which means a better prediction for the model. Although these three-performance metrics have been widely used when estimating model fitting, their values range was influenced by the values of data. Therefore, a single value of MAE, MSE and RMSE cannot be interpreted properly (Chicco et al., 2021).

The coefficient of determination (Equation 6) represents the proportion of the variance in the dependent variable that is predictable from the independent (Wright, 1921). It can evaluate the goodness of the model fitting. The closer the R-squared is to one, the better the model fits the data. R^2 does not need to be positive, however, if the value of R^2 is less than zero, it means the model is even worse than the mean value of all of the predicted LAI. Thus, the model is not good enough to use and the R^2 will be recorded as NA, which means not acceptable. R^2 of train data and R^2 of test data could also used to evaluate if the model was overfitting. If the difference between the R^2 values of the training and testing data was greater than 0.1, the model was considered a high risk of overfitting (Hawkins, 2004; Tetko et al., 1995).

Therefore, based on the performance metrics mentioned above, every model used a grid search method in order to obtain optimal hyperparameters, which could improve model performance. The main hyperparameters adjusted in the study were the number of the estimators and the maximin depth. The optimal hyperparameters were primarily determined by two factors. First, ensuring that the difference in R^2 value between the training set and the test set was less than 0.1. Otherwise, the smaller the better. Second, minimizing the RMSE or MAE in the test set. The changing of parameters might be changed several times until the model fitted the data well but not overfitting, and with the minimal error rate.

4. Result

4.1 Wheat height estimation from UAV data

Wheat height was estimated using UAV derived DSMs. The linear regression analysis performed between UAV data derived wheat heights and in-field measured heights did not include wheat on the first flight (April 5, 2023). The result revealed a strong positive correlation (Spearman correlation coefficient = 0.837) between the two variables. Moreover, with R^2 of 0.61 (Figure 8), the wheat height estimated by DSM data was highly indicative of actual wheat heights in the field. Therefore, UAV height data was reliable and the UAV techniques in estimating vegetation height were efficacy. The regression equation obtained from the model was:

$$y = 0.797x - 5.747 \qquad Equation\ 7$$

where y refers to the field height, $xand$ refers to the estimated height.

It indicated the tendency of the height based on UAV data to slightly underestimate field height, with a slope less than 1 (0.z797) and a negative y-intercept (-5.747).

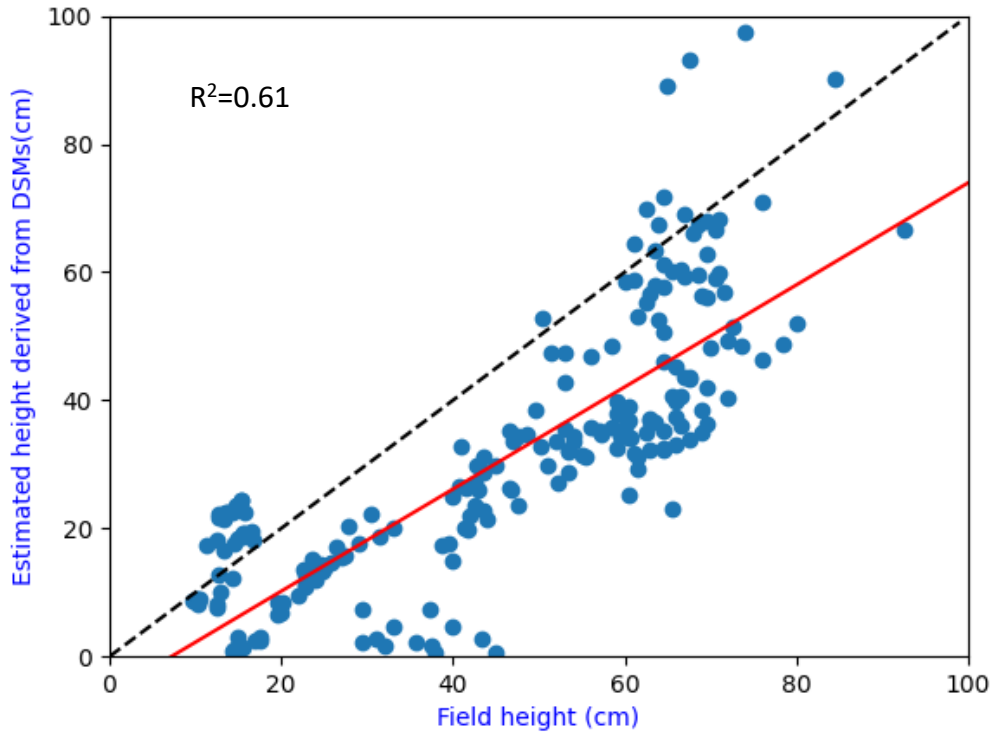

Figure 8. Estimated wheat height using digital surface models and measured wheat height. The red line is the fitted line and the dashed black line represents 1:1 line.

4.2 Time series analysis

The average LAI values computed from oblique images taken in 32 experimental points in each growth stage are shown in the box plots (Figure 9). From Figure 9 it can be observed that the LAI was dynamic across different growth stages. LAI values first increased gradually with the growth of wheat until it reached a peak at the booting stage. During the tillering stage, the LAI values are relatively low, indicating the initial phase of vegetative growth. The slope of LAI at the stem elongation stage shows that the mean LAI value increased quickly, suggesting leaves were developed at a quite high speed in this growth stage. The variability in LAI is high at this stage, indicating the great variability among individual plants. The booting stage marked the peak of LAI, with median and mean values exceeding 2.0, indicating the maximum leaf area development. From booting to ear emergence and flowering stage, LAI decreased very fast. Since this period was when wheat transferred from the growth stage to the mature stage. Subsequently, as wheat matured, the wheat leaves turned yellow and wither gradually, leading to a decline in LAI values. Eventually, at the ripening stage, all leaves turned yellow which meant there were no more green leaves on the wheat, therefore the LAI decreased to zero.

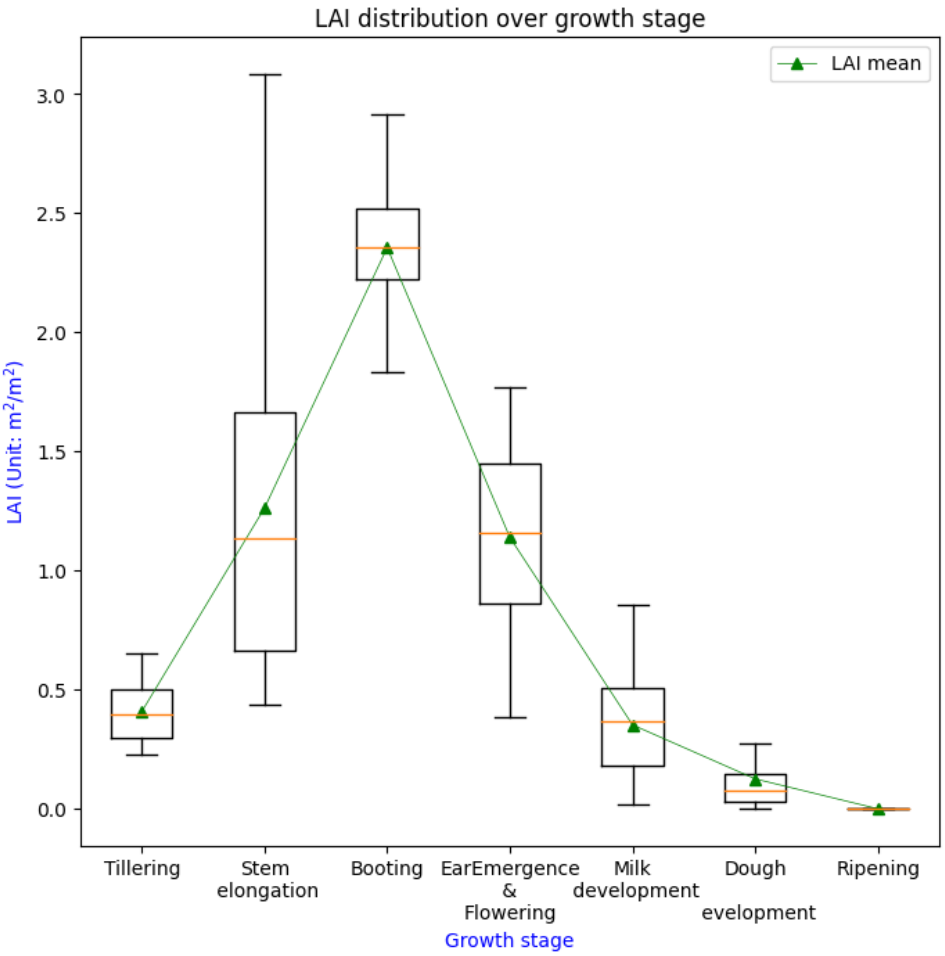

***Figure 9**. Boxplot graph of average LAI over the winter wheat growth stages in 2023. The horizontal line in orange indicates the median, each box indicates the interquartile range of LAI values, whiskers of each box indicate the maximum and minimum values (without outliers).*

For variables, Figure 10 displayed multiple line graphs representing the variations over growth stages. Different from the trend of LAI, the wheat height in field kept increasing until it reached the peak at the ear emergence and flowering stage. During subsequent growth stages, the plant height remained stable. UAV derived height measurements also exhibited a similar trend but with a lag in time, increasing continuously until reaching a peak slightly lower than field height measurements. Unlike the stability in plant height after reaching its peak, the NIR band showed a slow increase from the initial stage, reaching its peak at the booting stage. It then slowly decreased, with values at the maturity stage regressing to those at the tillering stage. The overall trend in NIR is consistent with LAI. REG band, however, remained

relatively stable throughout the growth stages, with minor fluctuations. There was no significant trend for REG values, which suggesting the consistent reflectance characteristics of the crop canopy, unaffected significantly by the growth stages.

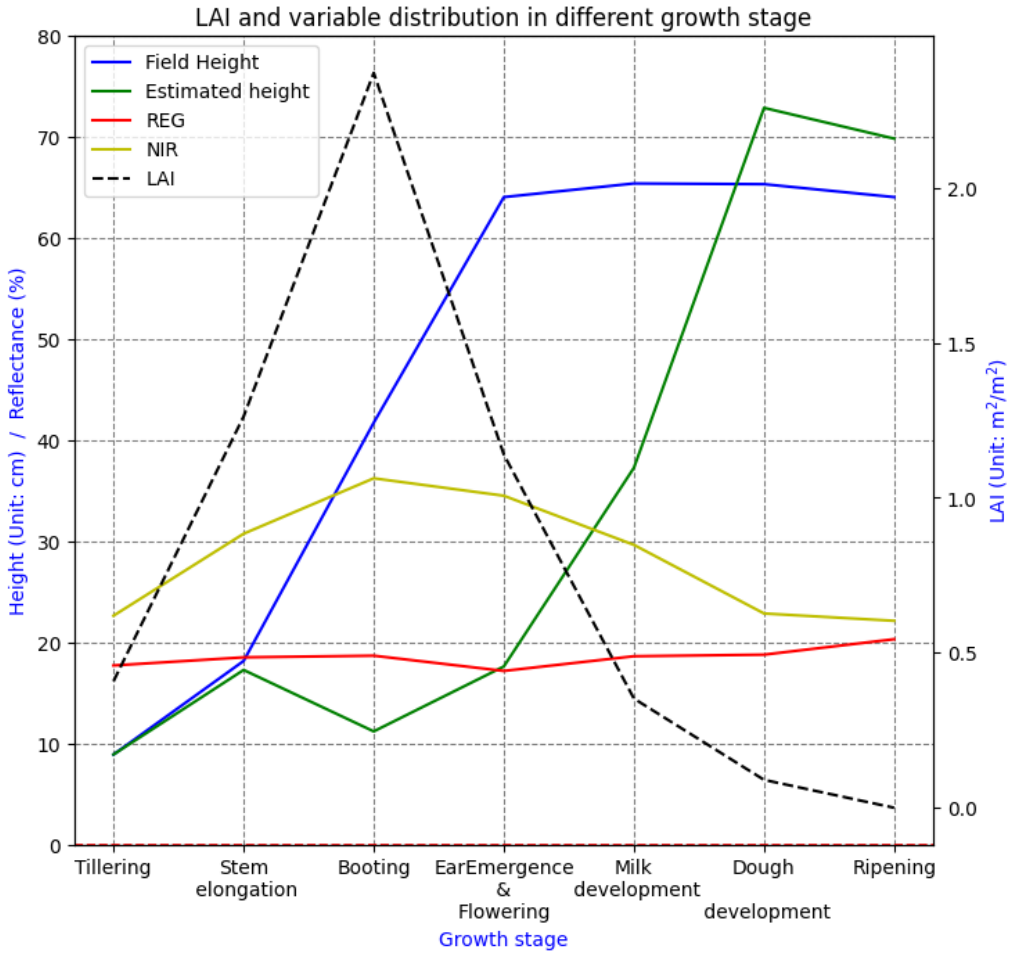

Figure 10. *Statistical line graph of reflectance of red-edge and near-infrared band, and height of winter wheat in time series in 2023. Field Height represents wheat height measured in the field. UAV Height is the wheat height estimated from UAV images.*

4.3 The correlation between LAI and variable

A total of were 234 samples used for analysing the correlation coefficient. As shown in Table 6 the correlation between REG and LAI was weak and negative (Spearman correlation coefficient = -0.134). The Spearman correlation coefficient for NIR was 0.698, reinforcing a moderate positive relationship between NIR and LAI ($p < 0.005$). Both VIs showed a strongly positive correlation with LAI (Spearman correlation

coefficient > 0.75). Height estimated from UAV exhibited a moderate negative correlation with LAI. The Pearson correlation coefficient was -0.309 ($p < 0.005$), and the Spearman coefficient was -0.260 ($p < 0.005$), suggesting that as UAV height increases, LAI tends to decrease. All variables except the height had a higher coefficient value in the Spearman correlation coefficient which double proved that the data was more like non-standard normally distributed. All p-values of the Spearman correlation were less than 0.05, so the results were statistically significant at 0.05 level.

Table 6*. Correlation analysis result between variable and LAI. Height is the wheat height estimated from UAV images.*

	Pearson correlation coefficient	**Pearson p-value**	**Spearman correlation coefficient**	**Spearman p-value**
REG	-0.096	0.145	-0.134	0.040
NIR	0.672	<0.005	0.698	<0.005
CIrededge	0.712	<0.005	0.786	<0.005
NDRE	0.738	<0.005	0.786	<0.005
Height	-0.309	<0.005	-0.26	<0.005

4.4 LAI estimation using single model

Modelling efforts to estimate LAI using individual features highlighted significant differences in model performance across various variables. In single model, a total of 223 data were used to train and test models.

When putting only one feature into the model, the result (Table 7) shows that using NDRE value to estimate LAI can lead to the best model performance (MAE = 0.425 m^2/m^2, RMSE = 0.540 m^2/m^2). The R^2 values reached 0.721 for training and 0.645 for testing, suggesting excellent model accuracy. On the opposite, the model utilizing REG values as a predictor exhibited limited predictive capability, as reflected in the highest errors (MAE = 0.803 m^2/m^2, RMSE = 0.899 m^2/m^2). In contrast, the other single band feature NIR demonstrated moderate effectiveness (R^2_train = 0.508, R^2_test = 0.403). It also had a lower error than REG which reflects a better estimation capability (MAE = 0.543 m^2/m^2, RMSE of 0.7 m^2/m^2). The errors with the use of CIrededge were slightly higher than NDRE (MAE = 0.47 m^2/m^2, RMSE of 0.597 m^2/m^2), but still showed a good model performance. The plant height-based model

also showed reasonable predictive power, with R^2 values of 0.394 in training and 0.334 in testing. The errors were moderate with MAE and RMSE at 0.593 and 0.739, respectively. Regarding model fitting, except REG, other models showed a reasonable model fitting. Since the difference between R^2_train and R^2_test was nearly lower than 0.1. For REG, the difference between R^2_train and R^2_test was 0.194, suggesting a high risk of overfitting. The primary reason for this overfitting was that the data characteristics were not suitable for the Random Forest algorithm. Or the data might be. Consequently, regardless of how the hyperparameters are adjusted, the models cannot achieve a good fit.

In summary, NDRE emerged as the most effective single feature for LAI estimation, demonstrating high reliability and accuracy. Conversely, REG reflectance showed significant limitations in its predictive capability.

Table 7. *LAI estimation results when using a single feature. REG and NIR are reflectance data after radiometric calibration. CIrededge and NDRE were computed based on the calibrated data. Height indicates the wheat height estimated from UAV images. The unit of MAE, MSE and RMSE is m^2/m^2.*

Single Feature	R^2_train	R^2_test	MAE	MSE	RMSE
REG	0.209	0.015	0.803	0.808	0.899
NIR	0.508	0.403	0.543	0.490	0.700
CIrededge	0.627	0.566	0.470	0.356	0.597
NDRE	0.721	0.645	0.425	0.291	0.540
Height	0.394	0.334	0.593	0.546	0.739

Based on the results above, the study extended the LAI model based on NDRE to estimate LAI for Field One across three different growth stages: tillering, booting, and dough development (Figure 11). The LAI map of Field One indicated a spatial variability in LAI. From the map on April 5, 2023, it could be observed that areas in the western part of the field had higher LAI values compared to the eastern areas. Additionally, wheat in the southwest corner showed a slower growth rate than the crops overall. This is particularly noticeable in the maps from May 21 and July 7, 2023.

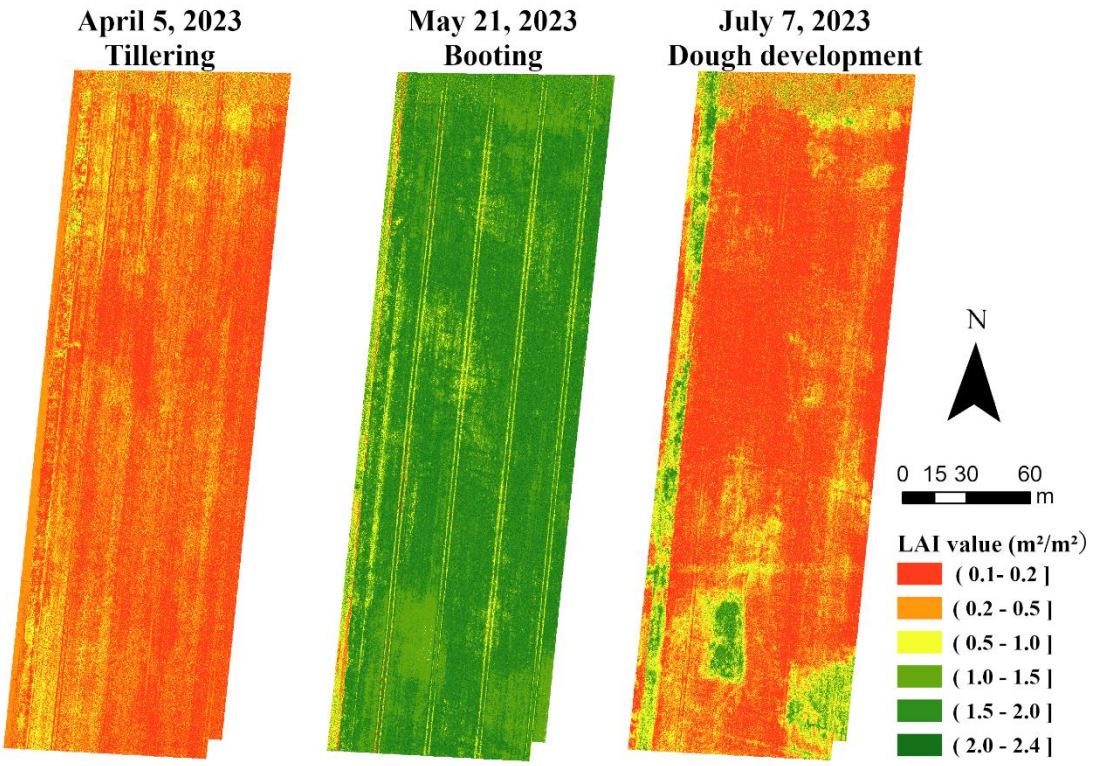

Figure 11. *LAI estimation map based on NDRE model in field one. Coordinates are displayed in the projected Coordinate System SWEREF99 TM.*

The result above suggested that combining multiple features could potentially enhance the accuracy of LAI estimation models, further analyses were conducted using combinations of height and spectral features. From the result (Table 8), the combined model of UAV Height with REG showed a slight improvement compared to single-feature models using REG alone but still had considerable error and variability. In contrast, the integration of UAV Height with NIR substantially enhanced model performance. The R^2 for training increased to 0.842 and to 0.785 for testing, suggesting good model fit and predictive power. Additionally, the model combining UAV Height I with VIs also showed highly favourable results. The combination of UAV Height and CIrededge achieved the highest predictive ability and the lowest error rates (R^2_train = 0.901, R^2_test = 0.829, MAE = 0.275 m^2/m^2, RMSE = 0.375 m^2/m^2).

Overall, models incorporating multiple features significantly enhanced the accuracy and reliability of LAI estimation. Specifically for the combinations of plant height with CIrededge.

Table 8. *LAI estimation results when using multi-features. REG and NIR are reflectance data after radiometric calibration. CIrededge and NDRE were computed based on the calibrated data. UAV Height indicates the wheat height estimated from UAV images. The unit of MAE, MSE and RMSE is* m^2/m^2.

Multi-features	R^2_train	R^2_test	MAE	MSE	RMSE
UAV Height + REG	0.371	0.318	0.645	0.559	0.748
UAV Height + NIR	0.842	0.785	0.318	0.177	0.420
UAV Height + CIrededge	0.901	0.829	0.275	0.141	0.375
UAV Height I + NDRE	0.893	0.811	0.283	0.155	0.394

4.5 Model based on growth stage

According to the temporal distribution of LAI (Figure 10), LAI increased continuously from tillering until booting, with a continuous decrease after. Therefore, to further analyse LAI estimation over growth stages, the study divided the growth cycle into two parts, using the booting stage as the boundary. The first part included the tillering, stem elongation and booting stages which were named periods of vegetative growth (Noggle, 1946). The second part included the rest of the growth stages (ear emergence, flowering, milk development and dough development), which were named periods of productive growth (Noggle, 1946). The ripening stage was not included in model development since the LAI value was zero. Data from these stages were randomly split in an 8:2 ratio to create training and testing subsets. The specific number of data used to train and test model is shown in Table 9.

Table 9. *Sample number of train data and test data for vegetative and productive stages.*

Data	Samples number	
	Vegetative stage	Productive stage
Total data	150	73
Train data	120	58
Test data	30	15

The estimation models for the vegetative stage demonstrated varying performance (Figure 12). NIR and VIs such as CIrededge and NDRE exhibited good prediction, with R^2 values on the training set being 0.666, 0.868, and 0.857, respectively (Table 10). The test results for CIrededge and NDRE maintained high R^2 values of 0.862 and

0.84, suggesting a good estimation ability. Conversely, REG had an R^2 of 0.121 in training and was not applicable (NA) in testing due to negative values, indicating poor model fit.

In the productive stage, the performance of all models generally decreased. VIs continued to perform best among the variables, with R^2 values of 0.858 and 0.847 for CIrededge and NDRE in training, and about 0.625 each in testing, respectively. NIR, while showing a good accuracy with an R^2 of 0.663 in training, dropped significantly to 0.018 in testing. Thus, the model was overfitted and NIR data was not a good option for estimating LAI in the productive stage.

In general, estimation accuracy decreased from the vegetative to the productive stages for all variables. CIrededge data can estimate LAI with the most accuracy, both in the vegetative to the productive stages.

Table 10. *LAI estimation results when using a single feature over growth stages. REG and NIR are reflectance data after radiometric calibration. CIrededge and NDRE were computed based on the calibrated data. Height indicates the wheat height estimated from UAV images. 'NA' refers to not applicable.*

	Vegetative stage		**Productive stage**	
	R^2_train	**R^2_test**	**R^2_train**	**R^2_test**
REG	0.121	NA	0.463	0.336
NIR	0.666	0.583	0.663	0.018
CIrededge	0.868	0.862	0.858	0.624
NDRE	0.857	0.840	0.847	0.625
Height	0.584	0.437	0.331	0.170

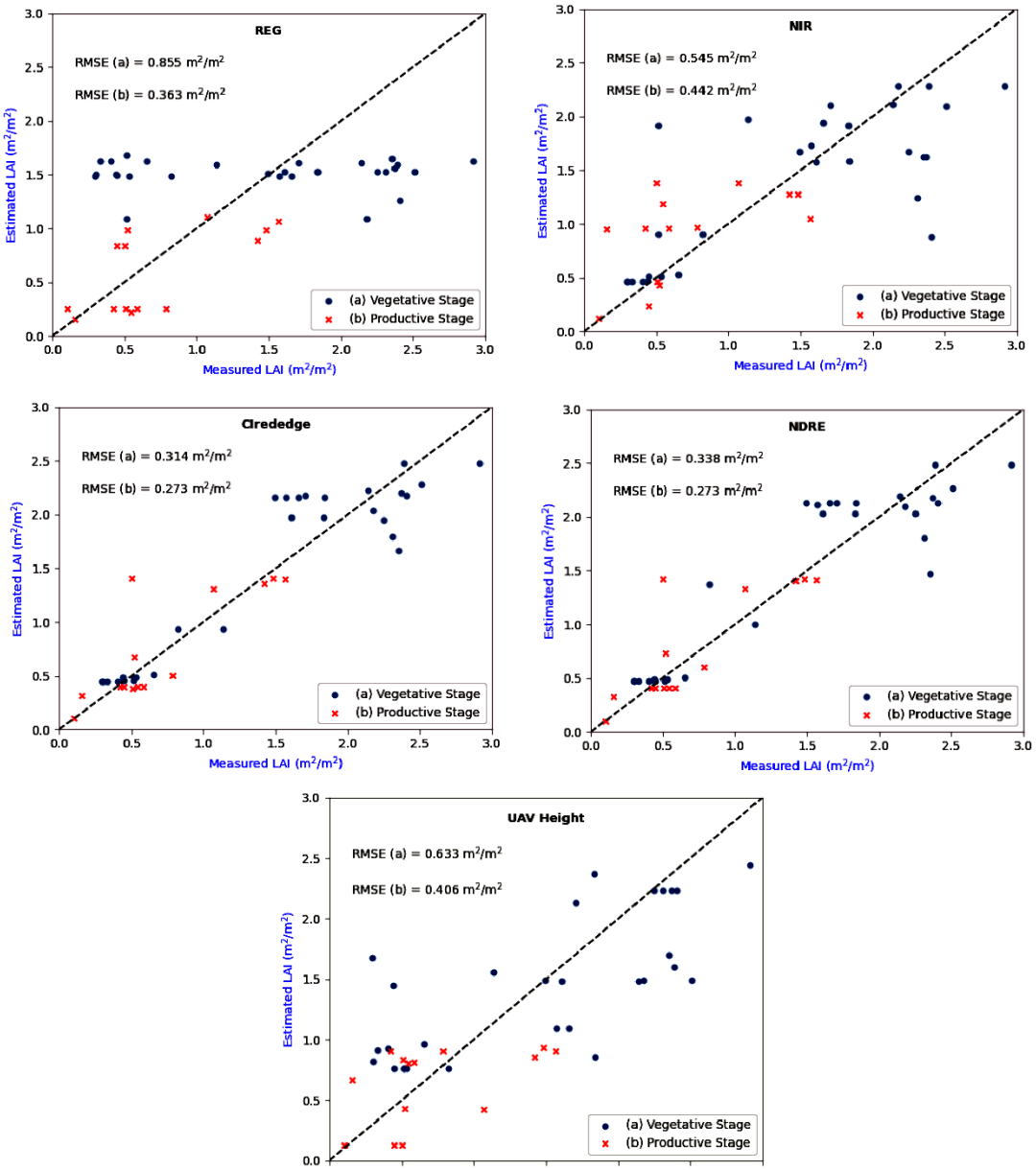

Figure 12. *Measured and estimated LAI in the vegetative stage (black dots) and productive stage (red cross. The dashed line indicates the ideal 1:1 relationship.*

5. Discussion

5.1 Weather impacts on LAI

Weather conditions can significantly impact the accuracy of LAI estimation. Cloud cover, for instance, can affect the quality of spectral data by reducing the effectiveness of the VIs. Besides, unstable weather conditions can introduce more noise and improve the challenge to calibrated ND values. Additionally, wind can cause crop movement, leading to blurred images and inaccurate height measurements. To avoid the influenced by the weather, UAV flights were scheduled during clear and calm weather conditions. And more weather relative data like humidity and wind speed could be considered when processing UAV images.

5.2 Uncertainties of plant height data

The plant height data in this study can be categorized into two parts. One is wheat height collected manually in the fields, which was used as the ground truth data. The other is wheat height estimated by DSM data processed from UAV images, which was used to establish LAI estimation models. And both parts have several factors which can contribute to the uncertainties of the plant height data.

For in-field data, the average height of four plants around each sample point was computed to represent the ground truth height at that sample point. However, the plant height had a variation in the field so the in-field data may contain errors. Additionally, field height was measured from the ground to the highest top of the plant manually. So, it was not influenced much by the change of ground height. However, the inconsistencies in ground surface height could cause a significant impact on the UAV-based wheat height estimation. There was a significant variety of ground surface height in different fields. Even the surface height of a small area of bare soil in the same position can have over 10 centimetres difference over two DSMs. Moreover, environmental factors might have an impact on plant height based on UAV estimation. For instance, strong winds could cause wheat to shift from an upright state to a tilted state. So, it was easy to see that the height from UAV estimation was always lower than the height from in-field measurement. Besides, since wind often occurs in gusts, it is challenging to maintain consistent plant surface heights during UAV image capture, resulting in a significant number of noise points in the collected data. Wind

also causes UAV platform vibration when acquiesced images (Jamil et al., 2022). The vibration affects the stability of sensors, which influences image mosaics (Zhang & Kovacs, 2012). These adverse conditions may decrease the quality of the dense point cloud, reduce the quality of the mesh, and result in higher errors during the generation of the DSM (Xie et al., 2021).

Thus, when using field height data as a reference, it is common to observe significant variability between the height estimated by UAV and the ground measurements. However, it is hard to define the source of the variety due to the uncertainties which made adjusting the height estimation models became very difficult.

5.3 Model overfitting

Overfitting is a common concern when developing predictive models (Ying, 2019). Model overfitting always happens when model learns noise in the training data instead of the underlying pattern, which leads to poor generalization on testing data or new data (Hawkins, 2004). Therefore, to prevent model overfitting, the study split the data into training and testing data sets and tried to restrict the difference of R^2 between training and testing sets lower than 0.1. However, for some models, it is nearly impossible to avoid overfitting. The possible reason is the data characteristics are not suitable for the Random Forest algorithm. Or the data might be insufficient. Therefore, in future research, different machine learning algorithms should be employed and the data should be expanded to avoid the problem of model overfitting.

5.4 The availability of REG band

From the result (Figure 10), the REG band was very stable throughout the study time. It also showed that there was nearly no practical relationship between REG and LAI (Pearson correlation coefficient = -0.096, Spearman correlation coefficient = -0.134). The weak correlations also suggest that any association might be due to the random change rather than a meaningful connection. Consequently, reliance on the REG band alone for LAI estimation resulted in significant errors. Additionally, the wavelength range of REG is narrow (730 nm ± 16 nm), and the reflectance of cereal farmland increases rapidly with increasing wavelength (Söderström & Persson, 2022). As a result, both environmental and sensor-related changes will be amplified, leading to a high level of noise in REG values. Analysis of Sentinel-2 REG reflectance (Band 5) data from November 2021 to October 2023 confirmed the absence of significant

trends (Figure 13), reinforcing the conclusion that the REG band should not be a primary consideration for LAI estimation. Despite this, the vegetation index CIrededge, derived from REG and NIR data, showed excellent performance during the productive growth stage. However, alternative vegetation indices not reliant on REG data might achieve comparable or superior performance.

Figure 13*. REG reflectance distribution over time, where the x-axis represents the date with format day. month. year, the y-axis represents reflectance. Data from Sentinel Hub (https://apps.sentinel-hub.com/eo-browser). Cloud coverage was 0%.*

5.5 Impaction of the radiometric calibration

Radiometric calibration is an important step when processing spectral data from drones. It converts DN to reflectance which describes the proportion of incident light that is reflected by the surface. The viewpoint regarding the unavailability of DN mainly focuses on that it is not a physical quantity but merely a numerical value (Dinguirard & Slater, 1999). Therefore, DN cannot be interpretable directly. DN values are also easily influenced by various factors including sensor characteristics, changes in observation conditions, and light intensity. So, it is meaningless when comparing DN values in different images. However, in this study, red, green and blue bands could not be calibrated. Therefore, only REG and NIR band was used to build the model which limited the choice of VIs. Therefore, the study analysed the possibility of using DN values to estimate LAI.

The distribution of DN value and reflectance of the sampling points are shown in Figure 14. When the reflectance is the same, the DN values often exhibit significant differences. The samples have a lower reflectance in the red edge band and are concentrated in the range from 15% to 20%. Reflectance is higher and more dispersed in the NIR band which is mostly distributed from 20% to 35%. Besides, for the DN value, the REG band displays a relatively narrow range (around 5000) when the reflectance is the same. But for one reflectance value, the range of DN value in the NIR band can show a variety of around 10000. Therefore, when using the DN value as the input data, due to deviations from actual reflectance, larger errors may result in the modelling. These errors might be more pronounced in the NIR band, since in the REG band, the distribution of DN values is relatively tight.

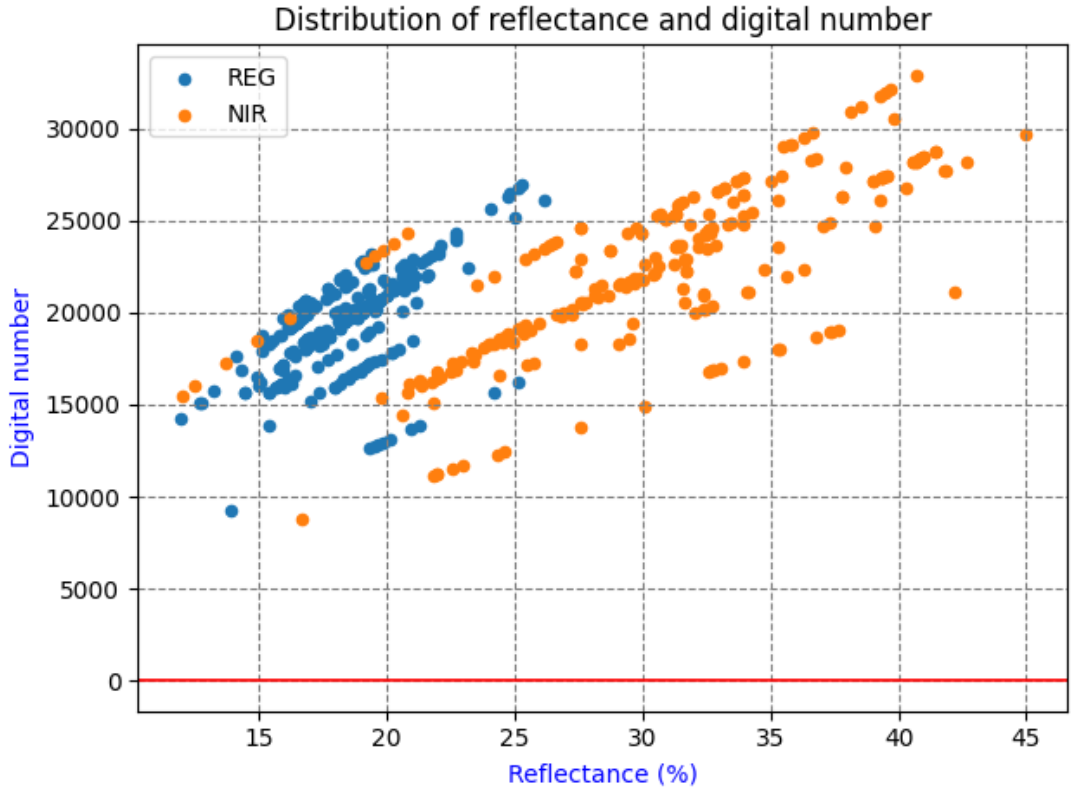

Figure 14. *Distribution of reflectance and digital number of red edge band and near-infrared band.*

When establishing one feature model with reflectance and DN value by using all data, the results indicated that the LAI estimating model based on reflectance had better model accuracy, with a higher R^2 and lower MAE and RMSE. The values of R^2 for testing data were below than 0.5 for all models, indicating the great error for all

models when estimating LAI. In summary, radiometric calibration is necessary and can improve model performance.

Table 11. *Model accuracy results when using a single feature. 'NA' refers to not acceptable.*

Single feature	R^2_train	R^2_test	MAE	MSE	RMSE
DN_REG	0.376	NA	0.803	0.846	0.920
DN_NIR	0.767	0.315	0.482	0.399	0.631
REG	0.209	0.015	0.803	0.808	0.899
NIR	0.508	0.403	0.543	0.490	0.700

Using DN values as data to estimate LAI requires ensuring that environmental factors remain as consistent as possible. For example, it is necessary to capture images at similar times of the day to ensure consistent light intensity, and to fly in cloudless conditions to ensure stable lighting. Furthermore, according to this study, adding the DN values of REG and NIR did not improve model accuracy. Using data from other bands and more effective vegetation indices may improve model performance. However, since DN is not a physical quantity, it may be difficult to interpret when the model shows an outlier result.

6. Conclusion

Estimating the LAI of winter wheat with high spatial resolution temporal flexibility ensures that critical information can be provided to farmers in a timely and precise manner. The main objective of the study was to comprehensively evaluate the efficacy of UAV-derived spectral and height data, with a high spatial resolution (4 cm × 4 cm), in estimating the LAI of winter wheat across various growth stages. The result indicated NDRE emerged as the most reliable single feature for LAI estimation, with an R^2 of 0.645 for testing, MAE of 0.42 m^2/m^2, and RMSE of 0.54 m^2/m^2. The inclusion of plant height data generally improved the accuracy and reliability of LAI estimation models. Multi-feature models demonstrated superior performance, with the combination of UAV height and CIrededge achieving the highest predictive accuracy and lowest error rates (R^2_test = 0.82, MAE = 0.27 m^2/m^2, RMSE = 0.37 m^2/m^2). Furthermore, temporal analysis of LAI showed LAI values peaking at the booting stage (average value of 2.37 m^2/m^2) and declining thereafter which provided additional insights into the distinct model performance variations between vegetative and productive stages. In the vegetative stage, CIrededge and NDRE exhibited high estimation accuracy, with R^2 values of 0.86 and 0.84 for testing data, respectively. In the productive stage, the model accuracy decreased, but CIrededge and NDRE remained the most effective features, with R^2 values of 0.62 and 0.62 for testing data. These growth stage-specific models suggested the importance of considering growth stages in LAI estimation to enhance model precision.

Overall, the study offered a robust approach for accurately estimating LAI in winter wheat. Future research should include data with a broader range of spectral wavelengths to compare more VIs, incorporate additional features into the model, and explore the application of these methodologies to other crops and environmental conditions to further validate and refine the models developed in this study.

Reference

Arkebauer, T. J. (2005). Leaf radiative properties and the leaf energy budget. *Micrometeorology in Agricultural Systems*, *47*, 93-103.

Ashourloo, D., Mobasheri, M. R., & Huete, A. (2014). Developing two spectral disease indices for detection of wheat leaf rust (Pucciniatriticina). *Remote Sensing*, *6*(6), 4723-4740.

Azadbakht, M., Ashourloo, D., Aghighi, H., Radiom, S., & Alimohammadi, A. (2019). Wheat leaf rust detection at canopy scale under different LAI levels using machine learning techniques. *Computers and Electronics in Agriculture*, *156*, 119-128. https://doi.org/https://doi.org/10.1016/j.compag.2018.11.016

Botchkarev, A. (2018). Performance metrics (error measures) in machine learning regression, forecasting and prognostics: Properties and typology. *arXiv preprint arXiv:1809.03006*.

Bréda, N. J. J. (2003). Ground-based measurements of leaf area index: a review of methods, instruments and current controversies. *Journal of Experimental Botany*, *54*(392), 2403-2417. https://doi.org/10.1093/jxb/erg263

Breiman, L. (2001). Random Forests. *Machine Learning*, *45*(1), 5-32. https://doi.org/10.1023/A:1010933404324

BUSH, T. F. (1976). Monitoring wheat growth with radar. *Photogrammetric Engineering and Remote Sensing*, *42*, 557-568.

Černý, J., Haninec, P., & Pokorný, R. (2020). Leaf area index estimated by direct, semi-direct, and indirect methods in European beech and sycamore maple stands. *Journal of Forestry Research*, *31*(3), 827-836. https://doi.org/10.1007/s11676-018-0809-0

Chai, T., & Draxler, R. R. (2014). Root mean square error (RMSE) or mean absolute error (MAE)? – Arguments against avoiding RMSE in the literature. *Geosci. Model Dev.*, *7*(3), 1247-1250. https://doi.org/10.5194/gmd-7-1247-2014

Cheng, Q., Ding, F., Xu, H., Guo, S., Li, Z., & Chen, Z. (2024). Quantifying corn LAI using machine learning and UAV multispectral imaging. *Precision agriculture*. https://doi.org/10.1007/s11119-024-10134-z

Chicco, D., Warrens, M. J., & Jurman, G. (2021). The coefficient of determination R-squared is more informative than SMAPE, MAE, MAPE, MSE and RMSE in regression analysis evaluation. *Peerj computer science*, *7*, e623.

Cort, J. W., & Kenji, M. (2005). Advantages of the mean absolute error (MAE) over the root mean square error (RMSE) in assessing average model performance. *Climate Research*, *30*(1), 79-82. https://www.int-res.com/abstracts/cr/v30/n1/p79-82/

Croux, C., & Dehon, C. (2010). Influence functions of the Spearman and Kendall correlation measures. *Statistical methods & applications*, *19*, 497-515.

Dinguirard, M., & Slater, P. N. (1999). Calibration of Space-Multispectral Imaging Sensors: A Review. *Remote sensing of environment*, *68*(3), 194-205. https://doi.org/https://doi.org/10.1016/S0034-4257(98)00111-4

Dong, C., Zhao, G., Qin, Y., & Wan, H. (2019). Area extraction and spatiotemporal characteristics of winter wheat–summer maize in Shandong Province using NDVI time series. *PloS One*, *14*(12), e0226508.

EuropeanCommission. (2024). *Agriculture database*. < https://ec.europa.eu/eurostat/web/agriculture/database>

Fang, H., Baret, F., Plummer, S., & Schaepman-Strub, G. (2019). An Overview of Global Leaf Area Index (LAI): Methods, Products, Validation, and Applications. *Reviews of Geophysics*, *57*(3), 739-799. https://doi.org/https://doi.org/10.1029/2018RG000608

Faye, B., Webber, H., Gaiser, T., Müller, C., Zhang, Y., Stella, T., Latka, C., Reckling, M., Heckelei, T., Helming, K., & Ewert, F. (2023). Climate change impacts on European arable crop yields: Sensitivity to assumptions about rotations and residue management. *European Journal of Agronomy*, *142*, 126670. https://doi.org/https://doi.org/10.1016/j.eja.2022.126670

Foley, W. J., McIlwee, A., Lawler, I., Aragones, L., Woolnough, A. P., & Berding, N. (1998). Ecological applications of near infrared reflectance spectroscopy–a tool for rapid, cost-effective prediction of the composition of plant and animal tissues and aspects of animal performance. *Oecologia*, *116*(3), 293-305.

Haboudane, D., Miller, J. R., Pattey, E., Zarco-Tejada, P. J., & Strachan, I. B. (2004). Hyperspectral vegetation indices and novel algorithms for predicting green LAI of crop canopies: Modeling and validation in the context of precision agriculture. *Remote sensing of environment*, *90*(3), 337-352. https://doi.org/https://doi.org/10.1016/j.rse.2003.12.013

Hauke, J., & Kossowski, T. (2011). Comparison of values of Pearson's and Spearman's correlation coefficients on the same sets of data. *Quaestiones geographicae*, *30*(2), 87-93.

Hawkins, D. M. (2004). The problem of overfitting. *Journal of Chemical Information and Computer Sciences*, *44*(1), 1-12.

Huang, S., Tang, L., Hupy, J. P., Wang, Y., & Shao, G. (2021). A commentary review on the use of normalized difference vegetation index (NDVI) in the era of popular remote sensing. *Journal of Forestry Research*, *32*(1), 1-6.

Jamil, N., Kootstra, G., & Kooistra, L. (2022). Evaluation of Individual Plant Growth Estimation in an Intercropping Field with UAV Imagery. *Agriculture*, *12*(1), 102. https://www.mdpi.com/2077-0472/12/1/102

JordbruksverketsStatistikdatabas. (2023). *Åkermarkens användning och antal företag med åkermark efter län och gröda.År 1981-2023.* < https://statistik.sjv.se>

Kanning, M., Kühling, I., Trautz, D., & Jarmer, T. (2018). High-Resolution UAV-Based Hyperspectral Imagery for LAI and Chlorophyll Estimations from Wheat for Yield Prediction. *Remote Sensing*, *10*(12), 2000. https://www.mdpi.com/2072-4292/10/12/2000

Kristensen, K., Olesen, J. E., & Schelde, K. (2011). Winter wheat yield response to climate variability in Denmark. *The Journal of Agricultural Science*, *149*(1), 33-47. https://doi.org/10.1017/S0021859610000675

Li, F., Miao, Y., Feng, G., Yuan, F., Yue, S., Gao, X., Liu, Y., Liu, B., Ustin, S. L., & Chen, X. (2014). Improving estimation of summer maize nitrogen status with red edge-based spectral vegetation indices. *Field Crops Research*, *157*, 111-123.

Li, F., Ren, J., Wu, S., Zhao, H., & Zhang, N. (2021). Comparison of regional winter wheat mapping results from different similarity measurement indicators of NDVI time series and their optimized thresholds. *Remote Sensing*, *13*(6), 1162.

Liu, C., Sun, P.-S., & Liu, S.-R. (2016). A review of plant spectral reflectance response to water physiological changes. *Chinese Journal of Plant Ecology*, *40*(1), 80.

Noggle, G. R. (1946). Some chemical changes associated with the transition from vegetative to reproductive growth of winter wheat. *Plant Physiology*, *21*(4), 492.

Olsson, P.-O., Vivekar, A., Adler, K., Garcia Millan, V. E., Koc, A., Alamrani, M., & Eklundh, L. (2021). Radiometric Correction of Multispectral UAS Images: Evaluating the Accuracy of the Parrot Sequoia Camera and Sunshine Sensor. *Remote Sensing*, *13*(4), 577. https://www.mdpi.com/2072-4292/13/4/577

Pôças, I., Calera, A., Campos, I., & Cunha, M. (2020). Remote sensing for estimating and mapping single and basal crop coefficientes: A review on spectral vegetation indices approaches. *Agricultural Water Management*, *233*, 106081.

Qi, J., Chehbouni, A., Huete, A. R., Kerr, Y. H., & Sorooshian, S. (1994). A modified soil adjusted vegetation index. *Remote sensing of environment*, *48*(2), 119-126.

Qiao, L., Zhao, R., Tang, W., An, L., Sun, H., Li, M., Wang, N., Liu, Y., & Liu, G. (2022). Estimating maize LAI by exploring deep features of vegetation index map from UAV multispectral images. *Field Crops Research*, *289*, 108739. https://doi.org/https://doi.org/10.1016/j.fcr.2022.108739

SCB. (2023). *Yield per hectar and total production in regions/country for different crops. Yearly data 1965 – 2022. Official Statistics of Sweden.* <https://www.scb.se/en/finding-statistics/statistics-by-subject-area/agriculture-forestry-and-fishery/agricultural-production/production-of-cereals-dried-pulses-and-oil-seeds>

Slafer, G. A., Savin, R., Pinochet, D., & Calderini, D. F. (2021). Chapter 3 - Wheat. In V. O. Sadras & D. F. Calderini (Eds.), *Crop Physiology Case Histories for Major Crops* (pp. 98-163). Academic Press. https://doi.org/https://doi.org/10.1016/B978-0-12-819194-1.00003-7

Söderström, M., & Persson, K. (2022). LEAF-PROXIMAL HYPERSPECTRAL DATA AND MULTIVARIATE MODELING: FROM DRONE TO SATELLITE–DOES IT WORK? 2nd African Conference on Precision Agriculture (AfCPA),

Steele, M. R., Gitelson, A. A., & Rundquist, D. C. (2008). A comparison of two techniques for nondestructive measurement of chlorophyll content in grapevine leaves. *Agronomy Journal*, *100*(3), 779-782.

Tetko, I. V., Livingstone, D. J., & Luik, A. I. (1995). Neural network studies. 1. Comparison of overfitting and overtraining. *Journal of Chemical Information and Computer Sciences*, *35*(5), 826-833. https://doi.org/10.1021/ci00027a006

Thapa, S., Garcia Millan, V. E., & Eklundh, L. (2021). Assessing forest phenology: a multi-scale comparison of near-surface (UAV, spectral reflectance sensor, phenocam) and satellite (MODIS, sentinel-2) remote sensing. *Remote Sensing*, *13*(8), 1597.

WATSON, D. J. (1947). Comparative Physiological Studies on the Growth of Field Crops: I. Variation in Net Assimilation Rate and Leaf Area between Species and Varieties, and within and between Years. *Annals of Botany*, *11*(1), 41-76. https://doi.org/10.1093/oxfordjournals.aob.a083148

Webber, H., Ewert, F., Olesen, J. E., Müller, C., Fronzek, S., Ruane, A. C., Bourgault, M., Martre, P., Ababaei, B., Bindi, M., Ferrise, R., Finger, R., Fodor, N., Gabaldón-Leal, C., Gaiser, T., Jabloun, M., Kersebaum, K.-C., Lizaso, J. I., Lorite, I. J., Manceau, L., Moriondo, M., Nendel, C., Rodríguez, A., Ruiz-Ramos, M., Semenov, M. A., Siebert, S., Stella, T., Stratonovitch, P., Trombi, G., & Wallach, D. (2018). Diverging importance of drought stress for maize and winter wheat in Europe. *Nature Communications*, *9*(1), 4249. https://doi.org/10.1038/s41467-018-06525-2

Williams, H., Colombi, T., & Keller, T. (2020). The influence of soil management on soil health: An on-farm study in southern Sweden. *Geoderma*, *360*, 114010. https://doi.org/https://doi.org/10.1016/j.geoderma.2019.114010

Wilson, J. W. (1960). Inclined point quadrats. *New Phytologist*, *59*(1), 1-7.

Wright, S. (1921). Correlation and causation. *Journal of agricultural research*, *20*(7), 557.

Xie, Q., Dash, J., Huang, W., Peng, D., Qin, Q., Mortimer, H., Casa, R., Pignatti, S., Laneve, G., & Pascucci, S. (2018). Vegetation indices combining the red and red-edge spectral information for leaf area index retrieval. *IEEE Journal of selected topics in applied earth observations and remote sensing*, *11*(5), 1482-1493.

Xie, T., Li, J., Yang, C., Jiang, Z., Chen, Y., Guo, L., & Zhang, J. (2021). Crop height estimation based on UAV images: Methods, errors, and strategies. *Computers and Electronics in Agriculture*, *185*, 106155.

Xue, J., & Su, B. (2017). Significant Remote Sensing Vegetation Indices: A Review of Developments and Applications. *Journal of Sensors*, *2017*, 1353691. https://doi.org/10.1155/2017/1353691

Yan, P., Han, Q., Feng, Y., & Kang, S. (2022). Estimating LAI for Cotton Using Multisource UAV Data and a Modified Universal Model. *Remote Sensing*, *14*(17), 4272. https://www.mdpi.com/2072-4292/14/17/4272

Yang, S., Peng, N., Zhai, D., Tao, Y., He, Q., Mu, X., Li, Y., & Fan, W. (2023). Fisheye-Based Forest LAI Field Measurements for Remote Sensing Validation at High Spatial Resolution. *IEEE Geoscience and Remote Sensing Letters*, *20*, 1-5. https://doi.org/10.1109/LGRS.2023.3308369

Ying, X. (2019). An overview of overfitting and its solutions. Journal of physics: Conference series,

Yu, T., Zhou, J., Fan, J., Wang, Y., & Zhang, Z. (2023). Potato Leaf Area Index Estimation Using Multi-Sensor Unmanned Aerial Vehicle (UAV) Imagery and Machine Learning. *Remote Sensing*, *15*(16), 4108. https://www.mdpi.com/2072-4292/15/16/4108

Zadoks, J., Chang, T., & Konzak, C. (1974). A decimal code for the growth stages of cereals. *Weed Research*, *14*(6), 415–421.

Zhang, C., & Kovacs, J. M. (2012). The application of small unmanned aerial systems for precision agriculture: a review. *Precision agriculture*, *13*, 693-712.

Appendix

App.1 Coordinates of the sampling spots

Table App.1 *Coordinates of the sampling spots. 'P' and the number along with it indicate the position number; numbers after the hyphen mean the sampling order in the position. The unit of the coordinates is in meters. The Projected Coordinate System is SWEREF99 TM.*

Field	Sample ID	East (m)	North (m)	Field	Sample ID	East (m)	North (m)
1	P01-1	378306	6169565	2	P9-5	380023	6169366
	P01-2	378330	6169563		P10-1	379956	6169428
	P01-3	378311	6169546		P10-2	379981	6169426
	P01-4	378326	6169525		P10-3	379972	6169406
	P01-5	378303	6169528		P10-4	379981	6169382
	P02-1	378296	6169460		P10-5	379956	6169383
	P02-2	378320	6169457	3	P17-1	378918	6168688
	P02-3	378300	6169438		P17-2	378954	6168685
	P02-4	378315	6169416		P17-3	378933	6168675
	P02-5	378292	6169418		P17-4	378949	6168650
	PST-W	378245	6169334		P17-5	378916	6168652
	P00	378276	6169475		P18-1	378879	6168558
2	P9-1	380023	6169413		P18-2	378904	6168555
	P9-2	380051	6169413		P18-3	378893	6168541
	P9-3	380039	6169388		P18-4	378899	6168523
	P9-4	380051	6169365		P18-5	378875	6168523